Porosity Formation in Al-9 Wt Pct Si-3 Wt Pct Cu Alloy Systems: Metallographic Observations

N. ROY, A.M. SAMUEL, and F.H. SAMUEL

The formation of porosity in Al-9 wt pct Si-3 wt pct Cu-X alloys was studied as a function of (1) the hydrogen content of the melt; (2) the melt treatment additives, namely, modifier (Sr), grain refiner (TiB_2), and primary silicon refiner (P); (3) alloying elements for precipitation hardening such as Mg and Zn; (4) intermetallics (α-iron, β-iron, sludge, and Al_2Cu); and (5) solidification conditions (solidification time and solidus velocity). The results were statistically analyzed, based on the quantitative image analysis data of the porosity observed in samples obtained from a set of 72 solidification experiments. Metallographic aspects of pore size and pore morphology related to the preceding parameters and the possible mechanisms of porosity formation are highlighted in this article. The results show that a melt hydrogen content of 0.1 mL/100 g Al has the same effect on percentage porosity as that obtained with an addition of 185 ppm strontium to the melt. Grain refiner particles, phosphorus, and magnesium reduce percentage porosity, although in different magnitudes. A Mg-Sr or Mg-GR combination further reduces the percentage porosity observed in the casting. The β needles of the Al_5FeSi intermetallic phase are very active as pore nucleation sites. All intermetallics, *viz.* β needles, α-Chinese script phase, Al_2Cu phase, and sludge restrict pore growth and expansion. Increasing the local solidification time or the solidus velocity increases the pore parameters. Pore growth in the two cases is attributed, respectively, to a diffusion-controlled growth process and to the formation of hot spots.

I. INTRODUCTION

POROSITY in aluminum alloy castings occurs because of the rejection of gas from the liquid metal during solidification and/or the inability of the latter to feed through the interdendritic regions to compensate for the volume shrinkage associated with the solidification.[1] Hydrogen is the only gas capable of dissolving to a significant extent in molten aluminum.[2] The dramatic decrease in its solubility at the solidification point of aluminum, resulting in outgassing, leads to the formation of porosity and reduced mechanical properties and corrosion resistance.[3,4,5]

Besides hydrogen concentration, the formation of porosity is also controlled by other factors such as grain refining and inclusion content. Grain refiners are added in small amounts to molten aluminum alloys to control the grain structure in the casting. Al-Ti and Al-Ti-B master alloys are usually employed, where $TiAl_3$ particles act as nucleation sites for the formation of primary α-aluminum dendrites and promote a uniform, equaxied grain structure. This leads to a finer dispersion of and, in some cases, a reduction in the amount of porosity.[6,7]

Modification of aluminum alloy melts is normally carried out to improve the mechanical properties. In Al-Si hypoeutectic alloys, it involves the addition of strontium or sodium to the melt in order to change the shape of the eutectic Si from acicular to fibrous.[8,9] The modified eutectic structure enhances the mechanical properties of the casting. However, this advantage is offset by the fact that modified castings generally exhibit an increased amount of porosity when compared to unmodified ones,[10,11,12] where the increased porosity can adversely affect these properties.[13,14]

The excellent foundry and mechanical properties of Al-Si-Cu alloys make them popular candidates for automotive applications. Based on the Al-Si system, these alloys contain copper and magnesium as the main alloying elements and varying amounts of iron, manganese, zinc, and other impurity elements that partly go into solid solution and partly form intermetallics during solidification. In the context of automotive applications, involving production of substantial amounts of castings, the porosity problem attains particular significance, and it becomes important to understand the development of porosity in relation to the various alloy, processing, and solidification parameters involved during the casting process.

As part of an ongoing research program on the study of porosity in important automotive alloys, porosity formation in Al-9 wt pct Si-3 wt pct Cu base alloys was studied, varying the additives (to cover the wide range of alloy compositions used in such applications), the hydrogen level, and the thermal parameters in order to obtain a statistical analysis of the resulting porosity in such alloy systems. The study was comprised of a set of 72 solidification experiments, where the pore size (area and length), morphology, and distribution were quantified using image analysis, as reported in detail elsewhere.[15,16] Tables AI and AII given in the Appendix summarize the results of these porosity measurements.

Metallographic aspects of porosity formation in these alloys related to the preceding factors are highlighted in this article. The microstructural observations presented throughout are typical representations of the statistically obtained data.

N. ROY, formerly Graduate Student, A.M. SAMUEL, Research Associate, and F.H. SAMUEL, Professor, are with the Department of Applied Sciences, University of Quebec at Chicoutimi, Chicoutimi, Canada G7H 2B1.

Manuscript submitted March 17, 1995.

Table I. Chemical Compositions of the Cast Alloys (Weight Percent—Obtained from ICP Analysis) and Hydrogen Content (mL/100 g Al)

Alloy	Si	Cu	Zn	Fe	Mg	Mn	Ti	Sr	P	H_2
f1	8.93	3.08	0.01	0.22	0.32	0	0.14*	0.013	0	0.22
f2	8.93	3.18	0.01	0.16	0.35	0.6	0.15*	0.023	0.0019	0.25
f3	8.93	3.19	0.10	1.19	0.31	0	0.15*	0.090	0	0.20
f4	8.93	3.31	0.06	1.06	0.33	0.62	0.14*	0.022	0	8.93
f5	8.93	3.23	0.7	0.19	0.29	0	0.137*	0.012	0.0033	0.25
f6	8.93	2.77	0.7	0.19	0.28	0.6	0.148*	0.014	0	0.31
f7	8.93	2.78	0.8	1.0	0.28	0	0.11*	0.014	0	0.31
f8	8.93	2.94	1.13	0.95	0.27	0.6	0.14*	0.015	8.93	0.25
h1	8.93	3.02	1.48	0.54	0.08	0.35	0.13	0.024	0	0.06
h2	8.93	3.32	1.51	0.60	0.09	0.20	0.19*	0.022	0	0.52
h3	8.93	3.06	1.49	0.55	0.08	0.30	0.13	0.017	0.0030	0.49
h4	8.93	3.05	1.47	0.55	0.08	0.28	0.14*	0.017	0.0033	0.13
h5	8.93	2.98	1.50	0.55	0.66	0.29	0.13	0.024	8.93	0.57
h6	8.93	3.41	1.56	0.57	0.77	0.26	0.19*	0.024	0	0.12
h7	8.93	3.68	1.56	0.57	0.61	0.36	0.14	0.017	0.0037	0.13
h8	8.93	3.12	1.47	0.53	0.66	0.30	0.19*	0.027	0.0011	0.45
s1	8.93	3.40	0	0.57	0.02	0.3	0.04*	0.002	0.0020	0.28
s2	8.93	3.16	0	0.56	0.01	0.3	0.27*	0.043	0.0025	0.24
s3	8.93	3.06	0	0.43	0.33	0.31	0.05*	0.042	0.0025	8.93
s4	8.93	3.35	0	0.53	0.24	0.3	0.29*	<0.002	0.0025	0.23
s5	8.93	2.84	1.8	0.56	0.01	0.31	0.03*	0.0300	0.0025	0.26
s6	8.93	2.90	1.9	0.79	0.01	0.31	0.09*	<0.002	0.0025	0.21
s7	8.93	3.16	1.7	0.54	0.67	0.3	0.03*	<0.002	0.0025	0.21
s8	8.93	2.87	1.8	0.97	0.30	0.3	0.06*	0.038	0.0025	0.29

*Grain refined with Al-5 pct Ti-1 pct B.

II. EXPERIMENTAL PROCEDURE

The base alloy, prepared from pure elements and containing Al-6 wt pct Si-3 wt pct Cu-0.15 wt pct Fe, was supplied in the form of 12.5-kg ingots by Alcan International's Kingston Research and Development Centre (Kingston, ON, Canada). The final composition was adjusted by adding Al-X master alloys (supplied by KB Alloys, Robards, KY), except in the case of Si, which was added in the form of pure metal (containing 15 ppm calcium). Table I shows the chemical compositions of the alloys used in the present work. These compositions were obtained from inductive couple plasma (ICP) analysis, carried out at Alcan International's Arvida Research and Development Centre (Jonquière, QC, Canada).

Alloys were melted in a silicon carbide crucible of 7-kg capacity using an electrical resistance furnace. The melting temperature was kept at 735 °C ± 5 °C. Two tapered wedge-shaped metallic molds were employed, one at an opening angle of 5 deg, heated at 40 °C (to avoid moisture pickup), and the other at 15 deg, heated at 300 °C. The inner surfaces of both molds were coated with thin layers of vermiculite to facilitate removal of the castings. Prior to casting, the molds were inclined at 35 deg with respect to the vertical position and then tilted up during pouring to minimize turbulence effects.

The melt hydrogen level was monitored using an AlScan unit, BOMEM, Inc., Québec (QC) Canada, G2E 5S5. In addition, specimens were cast simultaneously in a Ransley mold from which "Ransley" samples were machined for determination of hydrogen content employing the LECO* vacuum fusion technique, one of the standard methods for obtaining accurate analysis of the hydrogen content in a melt. The hydrogen concentrations obtained from the latter are listed in Table I.

The Ransley mold was originally invented by Ransley and Talbot to produce samples for measuring the hydrogen content of a melt from the solidified casting using a standard vacuum fusion technique. The mold is specially designed to prepare castings that are porosity free and which retain the hydrogen content of the melt in the solidified samples.[17] A typical Ransley mold is made of 1-in.-thick copper plates and weighs about 5.52 kg, while a casting obtained from it weighs about 260 g. The Ransley sample for hydrogen measurements is machined from the lower, cylindrical part of the casting, the larger, upper (riser) part being discarded. Prior to casting, the mold is dried by preheating it at 120 °C, and then allowing it to cool to a temperature above room temperature, to avoid moisture pickup. Cooling rates of the order of 30 °C/s are achieved with the mold.[18]

Metallographic samples were prepared from the various alloy castings. Porosity measurements were performed on polished sample surfaces at a magnification of 50 times so as to cover the entire sample surface. The porosity was quantified using a LECO 2001 image analyzer. Table II shows the average percentage surface porosity obtained for various alloy samples obtained at high and low cooling rates (corresponding to short and long solidification times (t_s) and designated small (S) and large (L) samples, respectively). For complete details of quantification and stastistical analysis, see References 15 and 16. Optical microscopic examination of porosity features was done on the polished sample surfaces (without etching), at different

*LECO is a trademark of LECO Corporation, St. Joseph, MI.

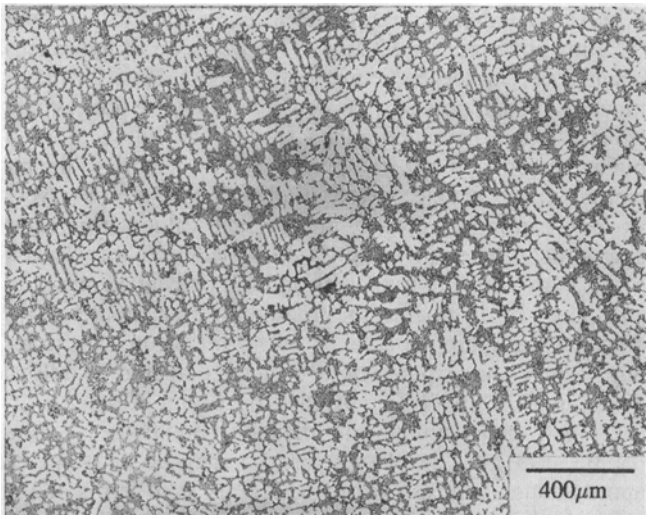

(*a*)

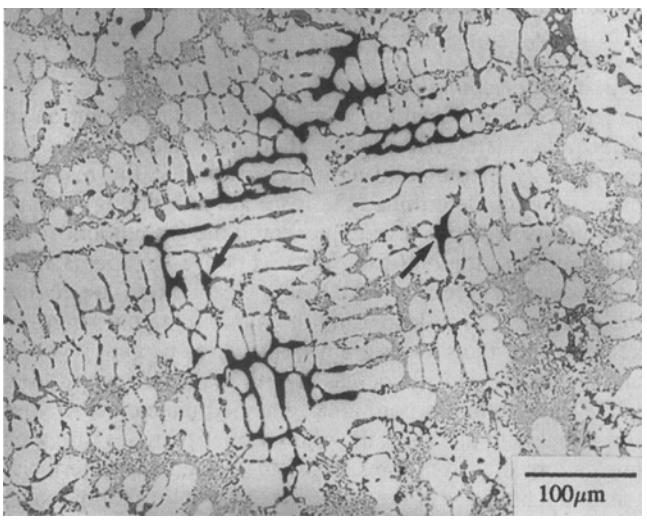

(*b*)

Fig. 1—(*a*) Pore distribution in h1S alloy (hydrogen content ~0.1 mL/100 g Al, t_s ~ 12.5 s). (*b*) A higher magnification micrograph of h1S alloy, showing small pores between dendrite arms.

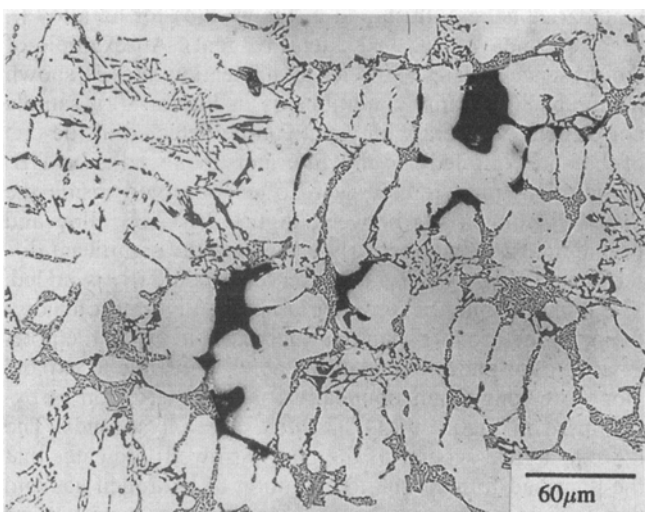

Fig. 2—Pores between dendrite arms in f5S alloy (hydrogen level ~0.25 mL/100 g Al, t_s ~ 12.5 s).

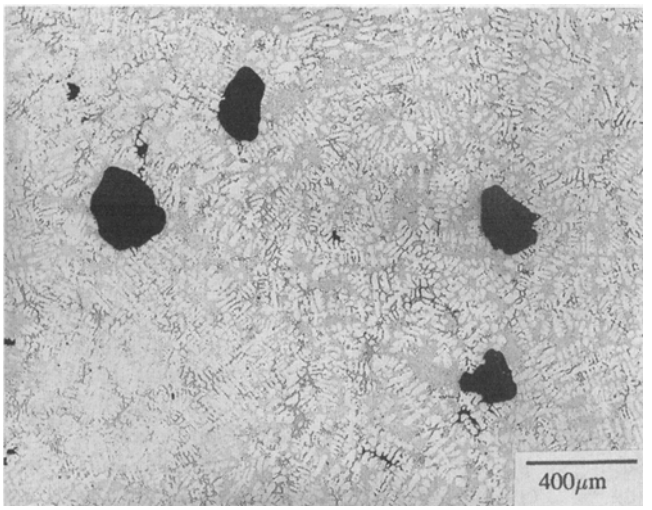

(*a*)

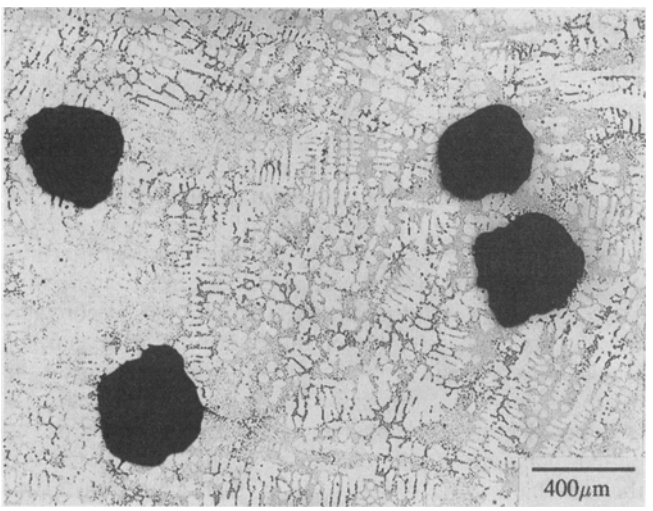

(*b*)

Fig. 3—(*a*) Pore morphology in h3S alloy (hydrogen content ~0.49 mL/100 g Al, t_s ~ 12.5 s). (*b*) Pore size and morphology in h3L alloy (hydrogen content ~0.49 mL/100 g Al, t_s ~ 71 s).

magnifications, using an Olympus PMG3 optical microscope.

III. RESULTS AND DISCUSSION

A. *Hydrogen*

At a very low hydrogen level, *i.e.*, 0.06 mL/100 g Al (h1 alloy), samples solidified at a high rate (solidification time, t_s ~ 12.5 seconds) exhibited almost no pores in the casting except for the central portion where fine pores were located along the dendrite arms. A typical example is displayed in Figure 1(a), with the high magnification micrograph of Figure 1(b) clearly showing the pores between the secondary dendrite arms. At a hydrogen level around 0.25 mL/100 g Al (f5 alloy), pores were seen to have the same shape as those depicted in Figure 1, only coarser in size, as shown in Figure 2.

In non-grain-refined alloy with a hydrogen content of about 0.49 mL/100 g Al (h3 alloy containing approximately 170 ppm Sr), elongated and rounded pores were observed

for $t_s \sim 12.5$ seconds, as demonstrated in Figure 3(a). Increasing the solidification time to ~71 seconds resulted in a significant change in pore morphology. Figure 3(b) reveals that all pores are almost rounded as opposed to the elongated form shown in Figure 2(b).

When the hydrogen content of the melt exceeds the solubility limit, the resultant excess hydrogen forms gas bubbles, leading to porosity. The pores nucleate and grow in the presence of proper nucleants,[1,16] their size and distribution depending on the local solidification conditions.[19,20,21] The porosity formation is described by the relation $\Delta P = 2\sigma/r$, where σ is the surface tension and ΔP is the critical pressure that must be exceeded in the pore for a pore nucleus of radius r to grow. A higher hydrogen content in the melt will increase ΔP and decrease r, resulting in an increase in the amount of porosity in the casting.[1,13] Pores may form prior to or during solidification. Pores of the former type are spherical (round) and relatively large. The ones formed during solidification are small, irregularly shaped (elongated), and attributed to shrinkage porosity. Their formation is influenced by the hydrogen enrichment and the shrinkage pressure in the interdendritic area.[22]

Figure 4(a) shows a spherical gas pore where the pore/matrix interface is mainly eutectic in h3 alloy ($t_s \sim$ 12.5 seconds). Increasing the solidification time (*i.e.*, 71 seconds) would lead to expansion of the pore toward the nearest dendrite arms, resulting in the change of the pore morphology to an oval shape, as evident from Figure 4(b) (note the presence of the intermetallic film on the pore surface). This process will continue until the pore surface touches the dendrite arms (Figure 4(c)). Depending on the hydrogen level and the size of the interdendritic region, a round/oval pore may cover over 20 dendrite arms, as depicted in Figure 4(d) for h5 alloy. It should be noted that this mechanism is different from that when two pores merge together to form one pore, as exemplified in Figure 5, where a gas (round) pore joins a shrinkage (elongated) pore.

B. *Melt Treatment*

1. *Modification (Sr)*

The influence of modification on porosity is a matter of considerable debate, stemming from the controversy over the behavior of Sr as modifier.[23] Argo and Gruzleski[7] carried out a controlled study on porosity in modified and unmodified A356 alloy (a higher purity version of 356 (Al-7 pct Si-0.35 pct Mg) alloy), using the Tatur test to identify differences in the distribution of porosity and shrinkage. The Tatur test uses a conical-shaped permanent mold of fixed geometry, where, with the use of simple density measurements, the volume of micro- and macroshrinkage, slumping, and contraction may be quantitatively evaluated. The radiographic data and Tatur results of Argo and Gruzleski[7] have shown that modification leads to a redistribution of porosity on solidification from the primary pipe type into microporosity, appearing thereby to increase the porosity. The results of Charbonnier *et al.*[24] on AS7G alloy (European version of A356) appear to agree well with their results.

Figure 6(a) shows the porosity distribution in unmodified s1 alloy (grain refined, hydrogen level ~0.23 mL/100 g Al, $t_s \sim 71$ seconds). Increasing the Sr content up to 130 ppm (f1 alloy containing a 0.22 mL/100 g Al level of hydrogen) resulted in a noticeable increase in the pore density without much change in pore size, as depicted in Figure 6(b), where isolated pores having rounded shapes can be seen. At a higher Sr content of 300 ppm (s5 alloy), noticeable increases in percentage porosity and pore size are observed, as shown in Figure 6(c) (*cf.* the average values of percentage porosity listed in Table II). It is evident that hydrogen plays a stronger role in increasing both percentage porosity and pore size compared to strontium. For example alloys containing a hydrogen level of ~0.49 mL/100 g Al exhibit higher percentage porosity, ~3 pct, compared to alloys containing 0.2 mL/100 g Al hydrogen and 430 ppm Sr, ~1.3 pct, under similar solidification conditions. Thus, a 0.1 mL/100 g Al level of hydrogen may be taken to be approximately equivalent to ~185 ppm Sr in terms of the effect on porosity formation (as measured by the percentage porosity). This observation is consistent with the features depicted in Figures 3(b) and 6(c) for h3 and s5 alloys, respectively.

2. *Grain refining (TiB_2)*

The work of Tynelius[25] on microporosity evolution in A356 alloy using a tapered wedge mold showed that the morphology of the solid-liquid interface and the resulting microstructure determined the resulting morphology of microporosity. The pores were present in the grain boundaries. Grain refiner addition (using Al-5 wt pct Ti-1 wt pct B alloy and measured in terms of 0.02 wt pct Ti addition) decreased the grain size, thus decreasing the maximum pore length in keeping with the shorter grain facets. Area percent porosity and areal pore density increased with grain refiner addition, while the maximum pore area remained unchanged. Tynelius concluded that the TiB_2 grain refiner particles provided nucleation sites for pores, without influencing interfacial tension. The latter is the parameter that controls pore size.

Figures 7(a) and (b) compare the porosity distribution in h2 and h3 alloys, respectively ($t_s \sim 71$ seconds). As reported earlier,[15] TiB_2 resulted in increasing nucleation sites as well as the number of grains, which led to a marked reduction in pore size with an increase in pore density (number of pores/cm^2). Nucleation of pores on the grain boundaries is best illustrated in Figure 8(a) for h2 alloy ($t_s \sim 71$ seconds, etched in Keller's reagent). An example of the presence of TiB_2 particles as nucleation sites is shown in Figure 8(b) (same conditions as in Figure 8(a), sample not etched), where a white spot can be detected inside one of the pores (circled). Such white spots, believed to be TiB_2 particles of grain refiner, were often observed inside the pores. A comparison between Figure 3(b)—h3 alloy and Figure 8(b)—h2 alloy clearly brings out the significant difference in pore size that is observed when TiB_2 is added. The higher magnification micrograph of Figure 8(c) shows the presence of more than one such particle inside the pore.

In the non-grain-refined alloy, pores were able to expand along the long grain boundaries. This observation is exemplified in Figure 9(a)—h3 alloy, $t_s \sim 71$ seconds. The more spherical section of the pore (arrowed) indicates that the pore had formed due to evolution of hydrogen gas and that the elongated morphology (or shrinkage-type part of the pore) is a consequence of the microstructure.[25] An example of the pores observed in grain-refined material (h2

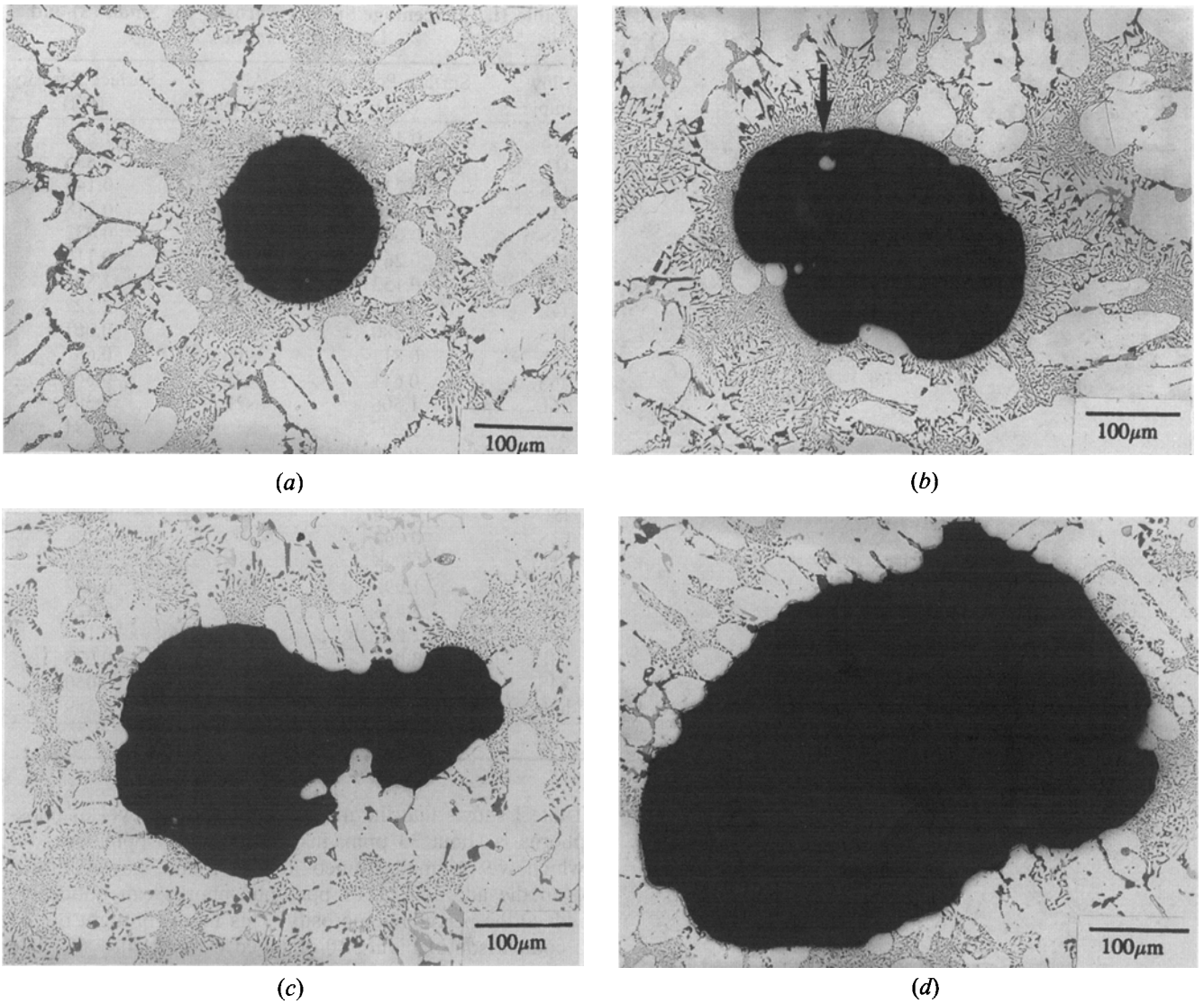

Fig. 4—(*a*) Gas pore nucleated within the interdendritic region in h3S alloy. (*b*) Expansion of gas pore in h3L alloy. (*c*) Change in pore shape from a spherical to an elongated form in h3L alloy. (*d*) A large elongated pore expanding over about 20 dendrite arms, h3L alloy.

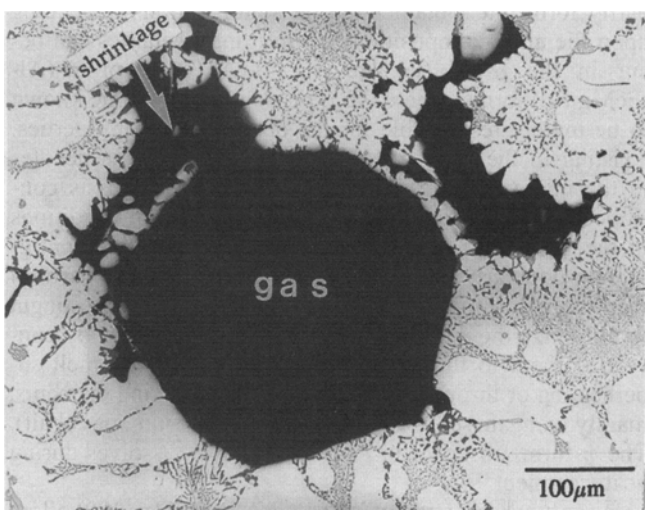

Fig. 5—A shrinkage pore and a gas pore merged together to form a single pore, h3L alloy.

alloy, t_s ~71 seconds), having a morphology similar to that observed in the non-grain-refined alloy, is shown in Figure 9(b). As can be seen, the pore length is strongly related to the intergranular structure, in particular, the grain boundary facet lengths, resulting in pore lengths that are markedly shorter.

3. *Silicon refining (P)*

Phosphorus enters aluminum casting alloy melts through contact with tools, refractories, refractory cements, or crucible glazes. In hypereutectic alloys, phosphorus is deliberately added because it reacts with the aluminum to form AlP particles which nucleate primary silicon. This results in a fine dispersion of primary silicon.[26] This effect is quite opposite to that observed in hypoeutectic alloys, where the silicon is coarsened by phosphorus addition. The reasons for such behavior, however, are not known.

Phosphorus, in the present work, was added as Cu-8 wt pct P brazing alloy. The aimed concentration, however, could not be achieved exactly. The chemical analysis in

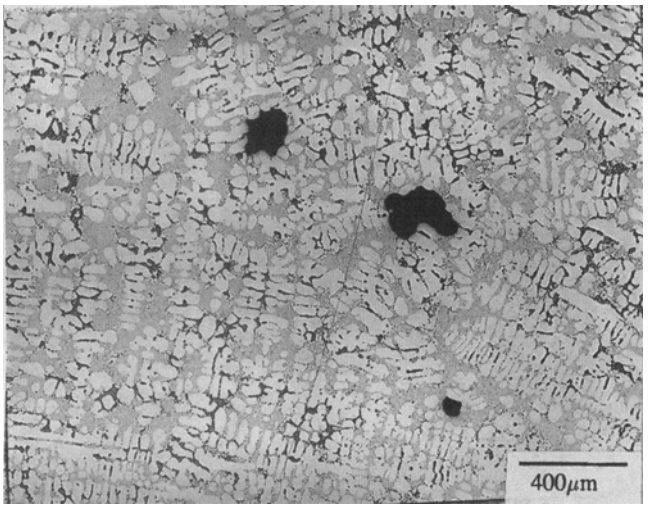

(*a*)

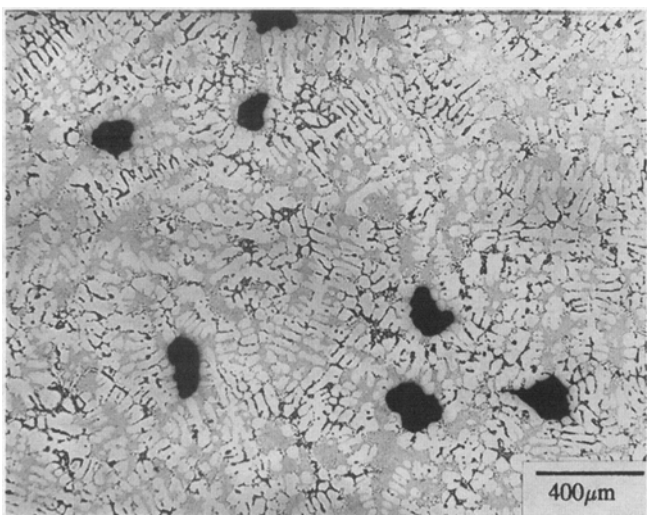

(*b*)

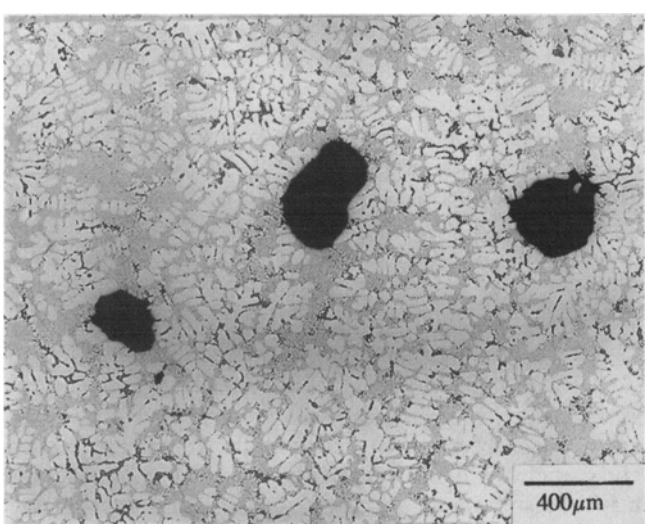

(*c*)

Fig. 6—Pore size and distribution in (*a*) s1L alloy—20 ppm Sr; (*b*) f1L alloy—130 ppm Sr; and (*c*) s5L alloy—300 ppm Sr.

Table II. Percentage Surface Porosity for Small (S) and Large (L) Samples

Alloy Sample	Surface Porosity (Pct)	Alloy Sample	Surface Porosity (Pct)
f1S	0.451	h5S	1.83
f1L	1.16	h5L	2.835
f2S	0.236	h6S	0.145
f2L	0.444	h6L	0.218
f3S	0.068	h7S	0.032
f3L	0.269	h7L	0.114
f4S	0.152	h8S	1.804
f4L	0.513	h8L	2.522
f5S	0.280	s1S	0.061
f5L	0.813	s1L	0.68
f6S	0.611	s2S	0.366
f6L	1.506	s2L	1.308
f7S	0.207	s3S	0.021
f7L	0.730	s3L	0.2466
f8S	0.260	s4S	0.062
f8L	0.396	s4L	0.282
h1S	0.064	s5S	0.358
h1L	0.094	s5L	1.285
h2S	1.99	s6S	0.042
h2L	2.433	s6L	0.624
h3S	2.25	s7S	0.11
h3L	3.066	s7L	0.675
h4S	0.044	s8S	0.060
h4L	0.065	s8L	0.389

S = t_s ~ 12.5 s; and L = t_s ~ 71 s.

Table I shows that the maximum attainable level of phosphorus is about 33 ppm, instead of the 60 ppm level for which we originally aimed. It was found, however, that even the addition of 19 ppm phosphorus can noticeably reduce the percentage porosity. This fact is brought out by a comparison of Figure 10 obtained from f2 alloy (t_s ~ 71 seconds) and Figure 6(b) produced from f1 alloy (t_s ~ 71 seconds).

C. *Intermetallics*

As mentioned previously, the various alloying and impurity elements in an alloy go partly into solid solution and partly form intermetallics during solidification. Depending upon the alloy composition, the iron intermetallics can occur in the α-($Al_{15}(Fe,Mn)_3Si_2$), β-(Al_5FeSi), or π-($Al_8FeMg_3Si_6$) forms, where the β phase is the only one known to be mainly responsible for the degradation in properties. Existing in the form of thin plates that appear as needles in the microstructure, the size of these β needles is controlled by the iron content and the solidification conditions of the alloy. The α form, having the skeleton-like configuration popularly termed "Chinese script," is less harmful than the β form of the iron phase, and it is always sought to minimize the detrimental effect of the β needles by converting them to the α form either by employing melt superheating or through the addition of neutralizing elements, mainly manganese (or also beryllium, chromium, or cobalt). The π form, observed in Al-Si-Mg alloys, dissolves during heat treatment.[27]

During solidification of Al-Si-Cu-Mg-Fe-Mn (380) alloy, of the type used in the present work, the following reactions are suggested to take place:[28]

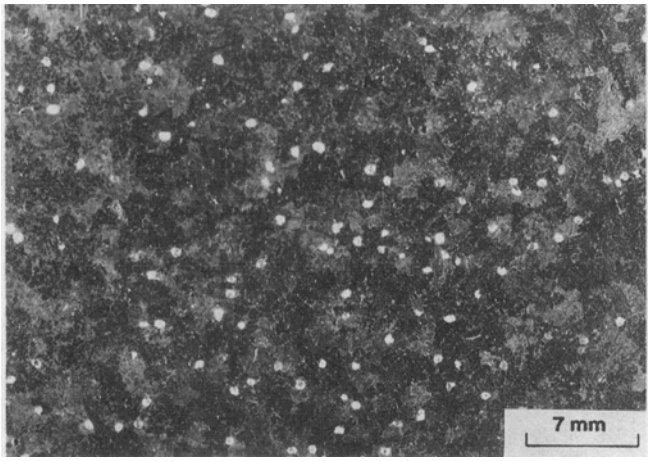

(*a*)

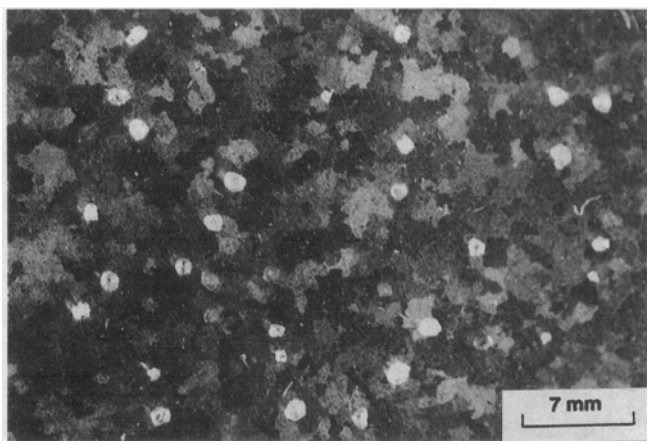

(*b*)

Fig. 7—Grain structure in (*a*) h2L alloy—grain refined; and (*b*) h3L alloy—nongrain-refined. Note pore size and distribution.

(1) development of a dendritic network (α-aluminum);
(2) precipitation of iron-containing phases (α-$Al_{15}(Fe,Mn)_3Si_2$ and β-Al_5FeSi);
(3) main eutectic reaction involving silicon and iron-containing phases;
(4) precipitation of Mg_2Si;
(5) precipitation of Al_2Cu; and
(6) formation of complex eutectics containing Al_2Cu and $Al_5Mg_8Si_2Cu_2$.

The sequence of precipitation or dominance of a specific iron-containing intermetallic is determined by the Fe:Mn ratio of the alloy.

1. *β-Al_5FeSi*

When the iron complex exists as long needles (β phase), it makes the alloy brittle and weak in mechanical properties. At the high cooling rates prevailing in the die-casting process, iron compounds are refined. An iron content up to 1.3 wt pct has been found to be beneficial in terms of improved strength, hardness, and tendency toward hot cracking.[29]

The pore distribution in f7 alloy (containing 1.2 wt pct Fe, $t_s \sim 71$ seconds) is shown in Figure 11(a). The pores are characterized by their elongated shape and very small length compared to the pores in f1 alloy (containing 0.22 wt pct Fe, $t_s \sim 71$ seconds), depicted in Figure 6(b). A

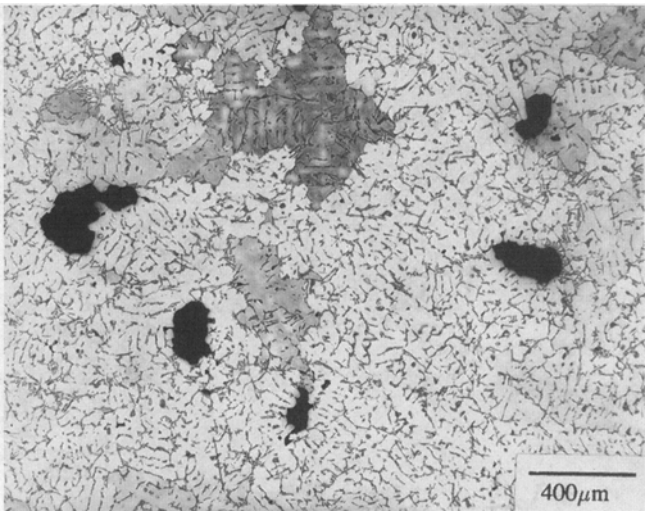

(*a*)

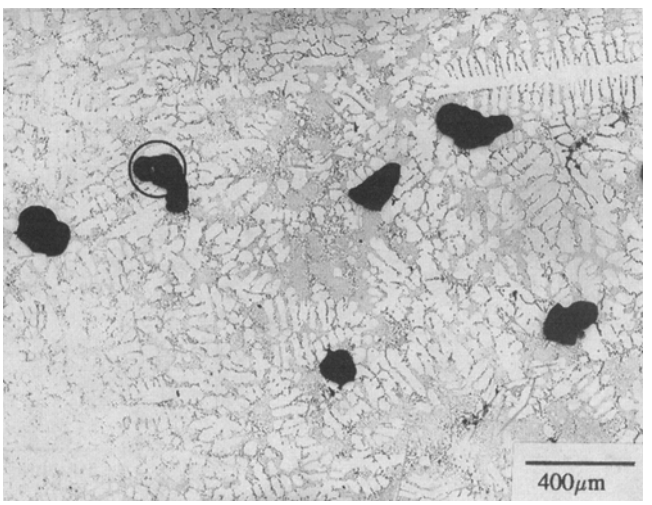

(*b*)

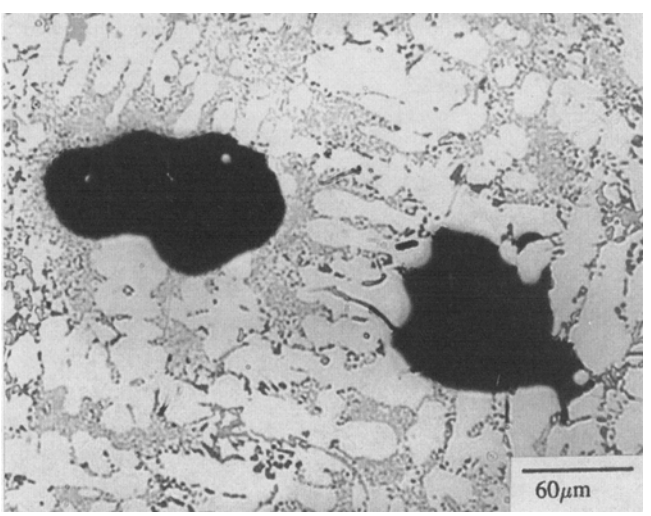

(*c*)

Fig. 8—(*a*) Nucleation of pores at grain boundaries and (*b*) pore size and distribution in h2L alloy. (*c*) A higher magnification micrograph of h2L alloy, showing inclusions inside the pores.

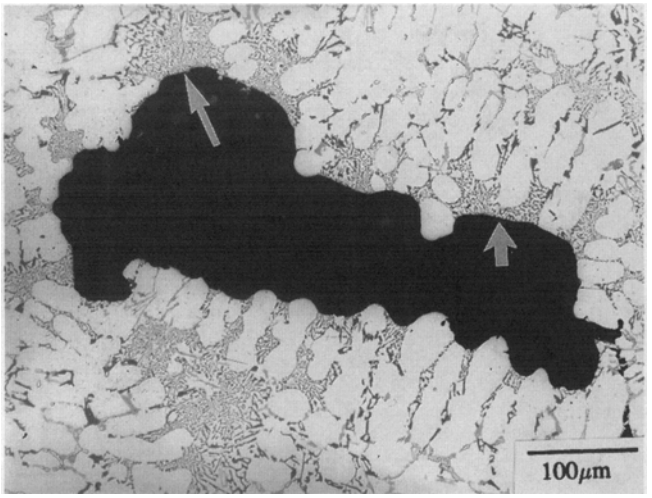

(*a*)

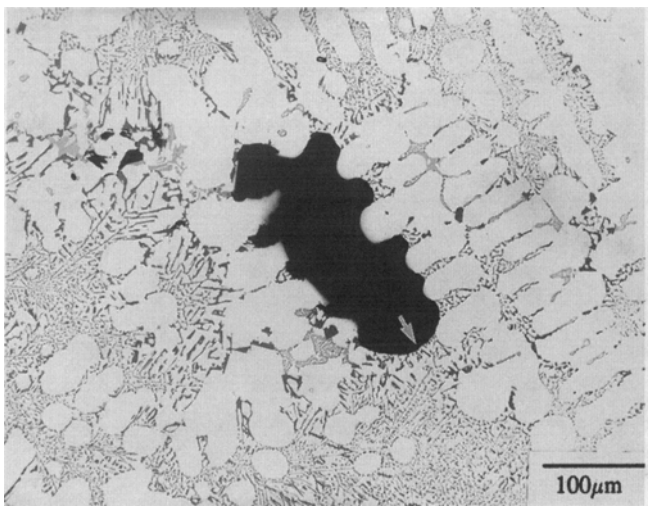

(*b*)

Fig. 9—Expansion of pores along the grain boundaries: (*a*) non-grain-refined h3L alloy and (*b*) grain-refined h2L alloy. Note how the dendrite arms extend into the pores.

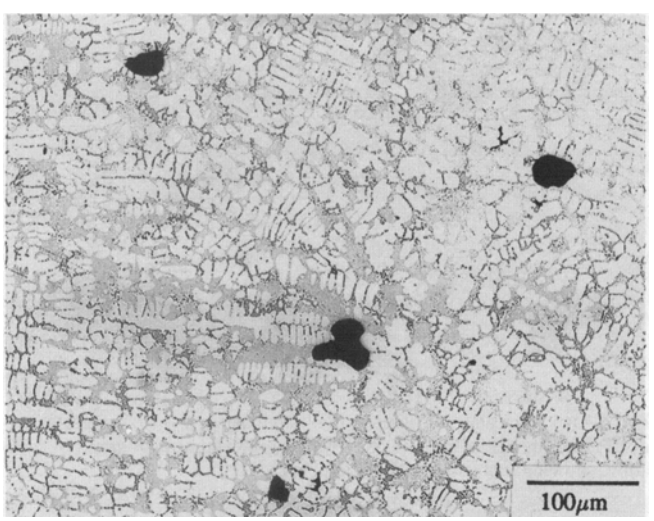

Fig. 10—Effect of phosphorus on pore size and distribution in f2L alloy.

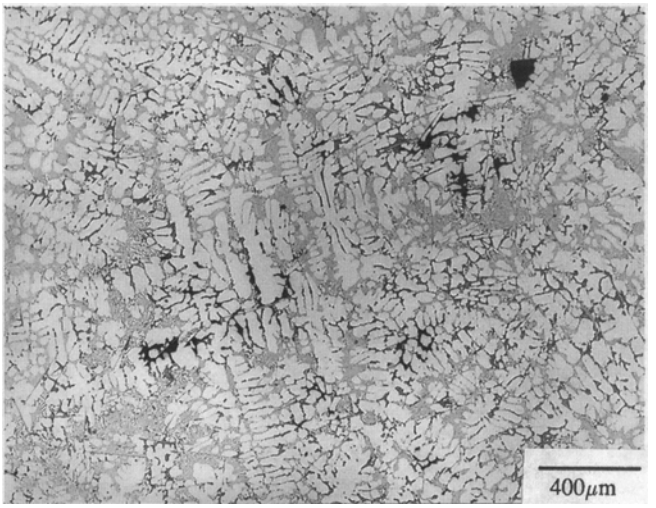

(*a*)

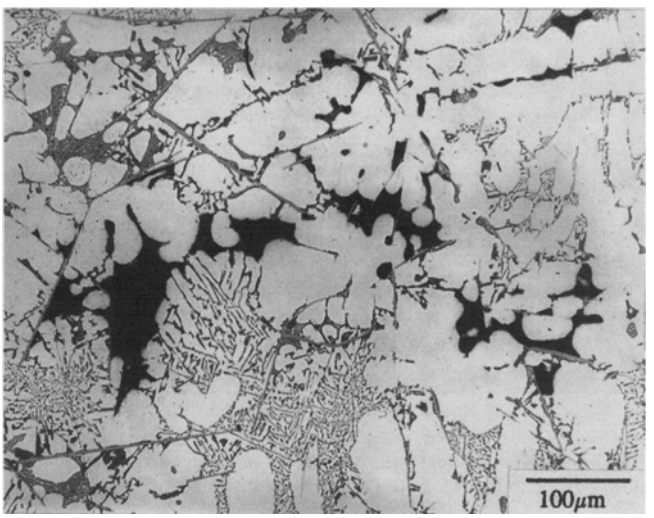

(*b*)

Fig. 11—Pore size and distribution in 1 wt pct Fe- containing f7L alloy: (*a*) general view and (*b*) nucleation of pores along the long sides of β needles.

higher magnification micrograph (Figure 11(b)) reveals that all pores are nucleated along the long sides of β needles. Such a mechanism is expected to result in an increase in pore density, which is strongly related to the metal feedability or the ease with which the molten metal can flow into the different sections of the casting mold.

In spite of the harmful effect of β needles as pore nucleation sites, their presence seems to limit pore growth. Figure 12(a) shows a gas pore formed within the interdendritic region, where its lateral growth is limited by the β needles on either side of the pore (as delineated by the small black arrows). In this case, the pores grow by advancing toward the nearest dendrite arms, as indicated by the white arrows in the figure. Similar observations are made in the case of shrinkage pores that nucleate at the grain boundaries (Figure 12(b)), the arrows highlighting the same aspects as those described in Figure 12(a).

2. α-$Al_{15}(Fe,Mn)_3Si_2$

The presence of iron in the Chinese script form is known to be relatively less harmful. As a rule of thumb, when the

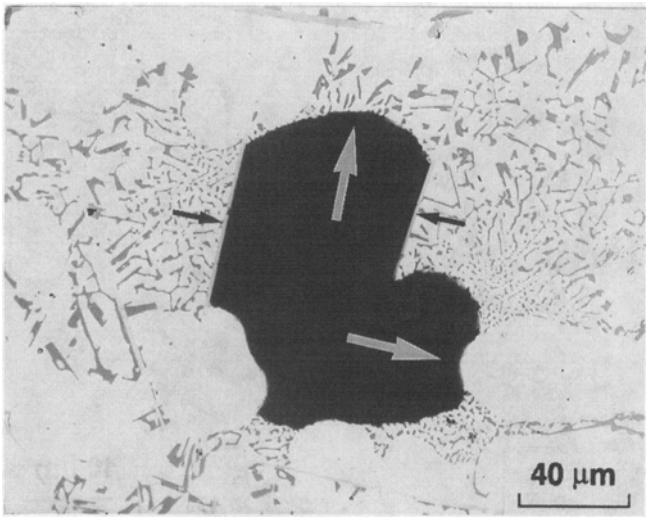

(*a*)

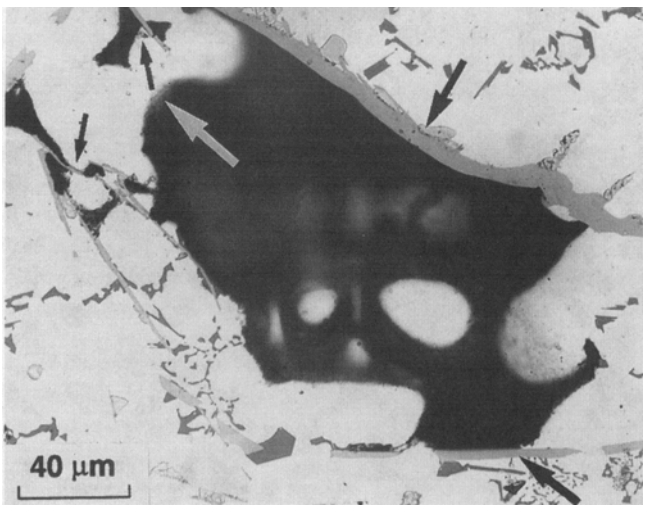

(*b*)

Fig. 12—Role of β-Al_5FeSi needles in restricting the growth of (*a*) a gas pore and (*b*) a shrinkage pore. Note the presence of small pores along the long sides of the β needles, delineated by the short arrows.

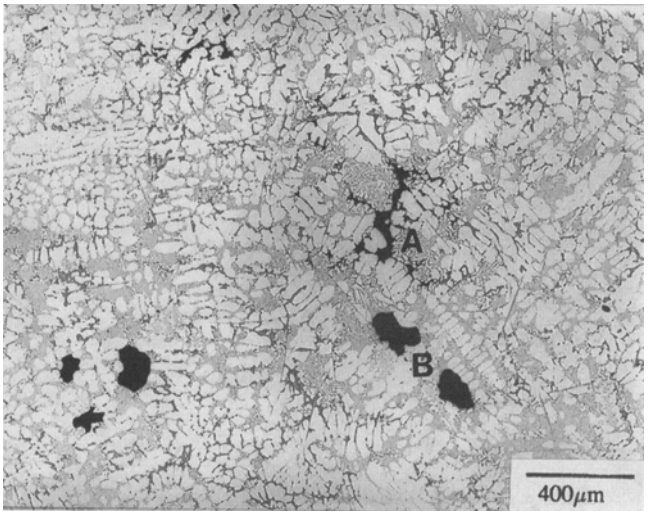

(*a*)

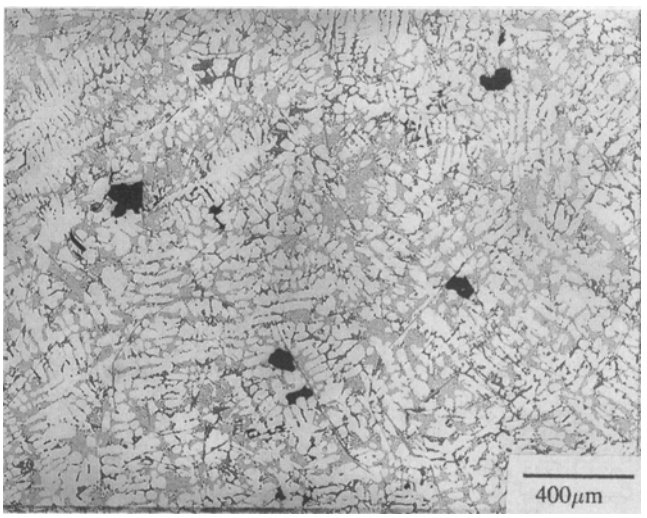

(*b*)

Fig. 13—Effect of Mn in neutralizing β-Al5FeSi needles: (*a*) 0.35 wt pct Mn-containing alloy and (*b*) 0.67 wt pct Mn-containing alloy. Note the mixture of shrinkage (marked A) and gas pores (marked B) in the low Mn-containing alloy.

iron content exceeds 0.45 wt pct in sand and permanent mold castings, the iron:manganese ratio is maintained at 2:1.[30]

Figure 13(a) exhibits the pore form and distribution in f8' alloy with low manganese content (Mn ~0.35 wt pct, t_s ~ 71 seconds). This alloy is not shown in Table I, since the manganese content was accidently obtained lower than the 0.6 wt pct level for which we aimed. With an iron concentration of ~1.1 wt pct, however, the iron:manganese ratio is ~3.1, which is higher than that required to neutralize all β needles. As a result, although a clear difference in pore size and distribution can be seen as compared to Figure 11(a), the pores are nevertheless still seen to nucleate on the sides of the remaining β needles (*cf.* Figures 6(c) and 11(a)). Increasing the manganese level in this alloy to 0.6 wt pct (which is the correct composition for f8 alloy) resulted in more or less complete elimination of β needles and, hence, the mechanism of pore nucleation depicted in Figure 13(b). The higher magnification micrographs presented in Figures 14(a) and (b) for the f8 alloy (t_s ~ 71 seconds) support the conclusion that α-Chinese script phase particles are not suitable sites for pore nucleation. Also, they highlight the fact that these particles are effective in limiting pore growth (Figure 14(b)).

3. *Sludge*

Manganese is always considered in relation to iron in foundry alloys. At low holding/casting temperature, the manganese combines with iron and chromium (Cr always exists as one of the impurities) to form sludge. Sludge is harmful as it is hard and abrasive. The sludge factor (SF) allowance is around 1.8 and is defined as SF = 1 × (Fe wt pct) + 2 × (Mn wt pct) + 3 × (Cr wt pct).[31]

The microstructure shown in Figure 15(a) was obtained from f8 alloy (t_s ~ 71 seconds) and reveals that sludge acts in a similar manner as the α-Chinese script particles in restricting pore expansion. Also, it is not an active pore nucleation site compared to β needles, as shown in Figure 15(b).

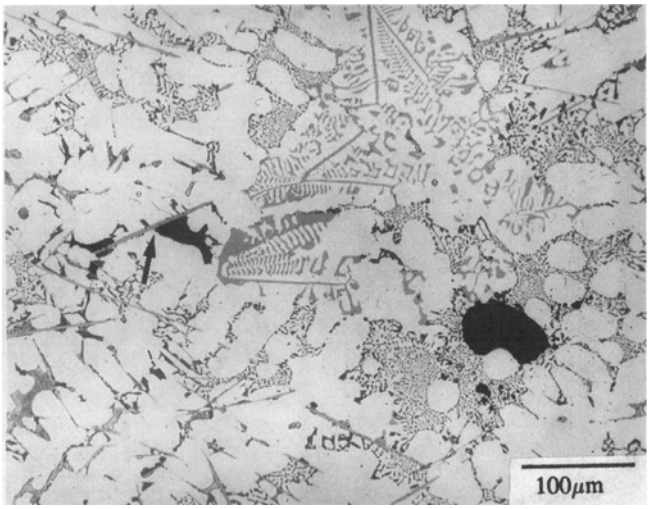

(a)

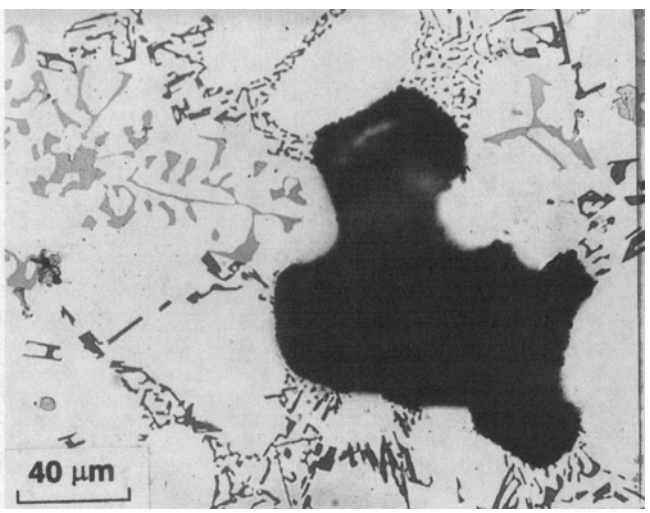

(b)

Fig. 14—(a) Difference in the role of β-Al_5FeSi needles and α-Chinese script phase particles on pore nucleation. (b) Role of α-Chinese script phase particles in restricting pore expansion in f8L alloy.

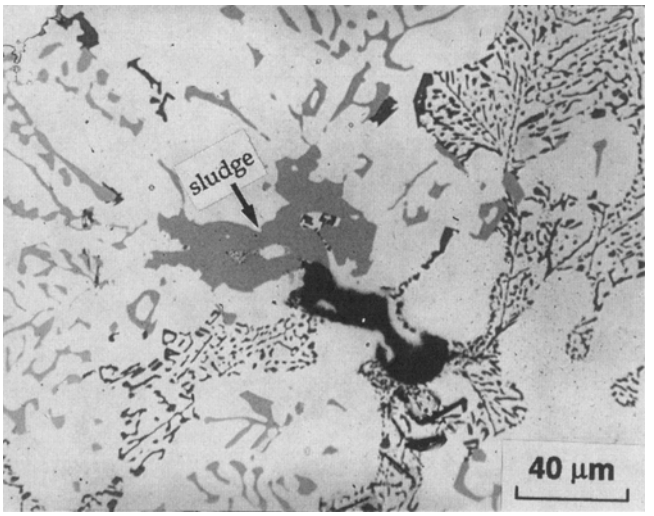

(a)

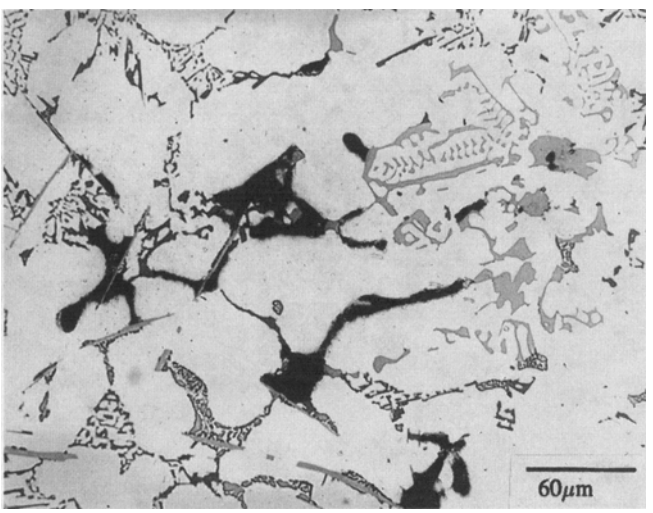

(b)

Fig. 15—(a) Role of sludge in limiting pore growth in f8L alloy. (b) A comparison between the three iron-containing intermetallics on their effect on pore nucleation or in limiting pore expansion.

4. *Al_2Cu*

The addition of copper to Al-Si alloys improves the strength of the castings.[29] Copper in these alloys is present as Al_2Cu or in a complex form. Depending on the cooling rate and strontium level, Al_2Cu phase appears in the microstructure in blocky form, or as a fine (Al + Al_2Cu) eutectic colony, or in both forms simultaneously.

In materials containing a very low level of hydrogen, *i.e.*, h1 alloy (hydrogen level ~0.06 mL/100 g Al, t_s ~ 71 seconds), shrinkage pores are seen to nucleate at the interface of blocky Al_2Cu-phase particles, as shown in Figure 16(a). As reported earlier,[32] strontium modifies the Al_2Cu-phase particles, resulting in more (Al + Al_2Cu) eutectic pockets. From Figure 16(b), obtained from f5 alloy (Fe ~0.2 wt pct, hydrogen content ~0.25 mL/100 g Al, t_s ~ 71 seconds), it is seen that in the absence of β needles, these eutectic pockets can be considered as pore nucleation sites. They are, however, very much less active compared to the β needles (Figure 16(c) for s6 alloy).

D. *Alloying Elements*

1. *Magnesium*

In North America, the allowable magnesium concentration in Al-Si-Cu base foundry alloys is 0.1 wt pct maximum, whereas European specifications allow 0.3 wt pct maximum. In spite of the studies reported in the literature that establish the beneficial effect of increasing magnesium on the mechanical and machining properties,[33–36] the specification still remains at 0.1 wt pct maximum.

The pore size and distribution in s7 alloy (containing 0.67 wt pct Mg, hydrogen level ~0.21 mL/100 g Al, t_s ~ 71 seconds) are presented in Figure 17(a). From Table II, and Figures 6(b) and 17(a), it is seen that the addition of magnesium reduces percentage porosity without a noticeable change in pore size or shape. The role of magnesium in reducing percentage porosity is more pronounced when the hydrogen content is increased to ~0.5 mL/100 g Al. This is shown in Figure 17(b) obtained from h5 alloy (hydrogen level ~0.57 mL/100 g Al, t_s ~ 71 seconds) as com-

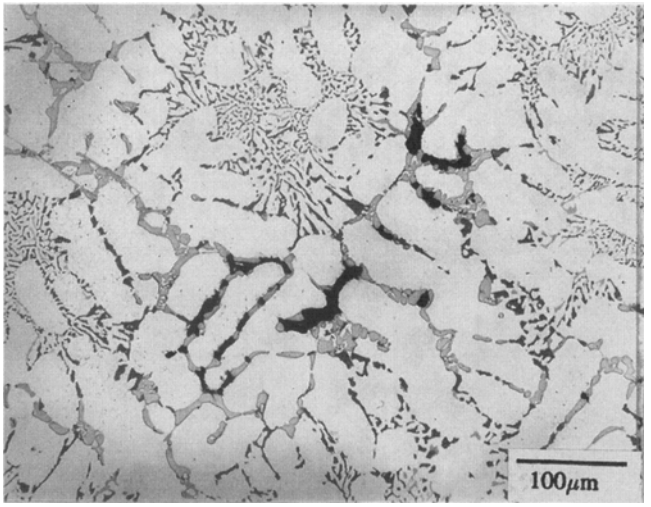

(*a*)

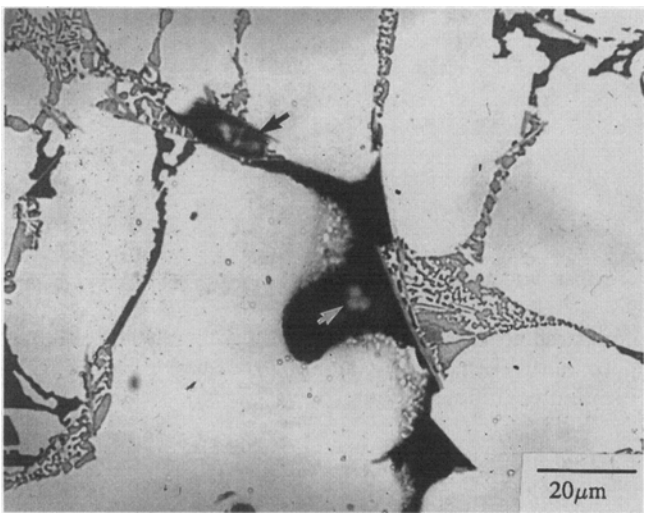

(*b*)

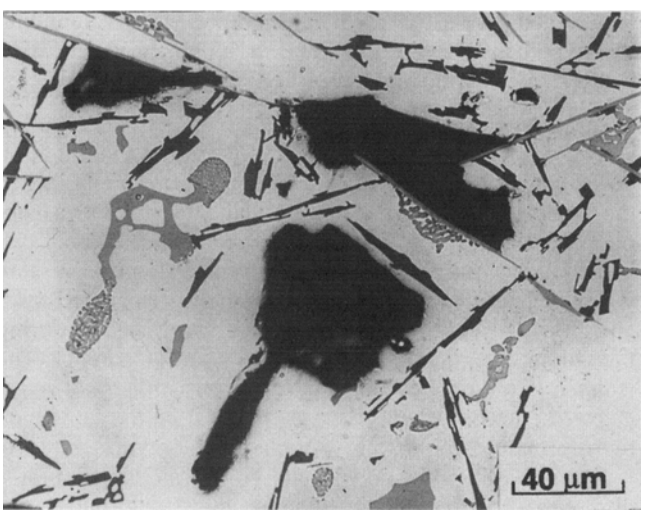

(*c*)

Fig. 16—Role of Al_2Cu phase particles as sites of pore nucleation in: (*a*) h1L alloy, (*b*) f5L alloy, and (*c*) s6L alloy. Note the presence of nonmetallic inclusions inside the pores.

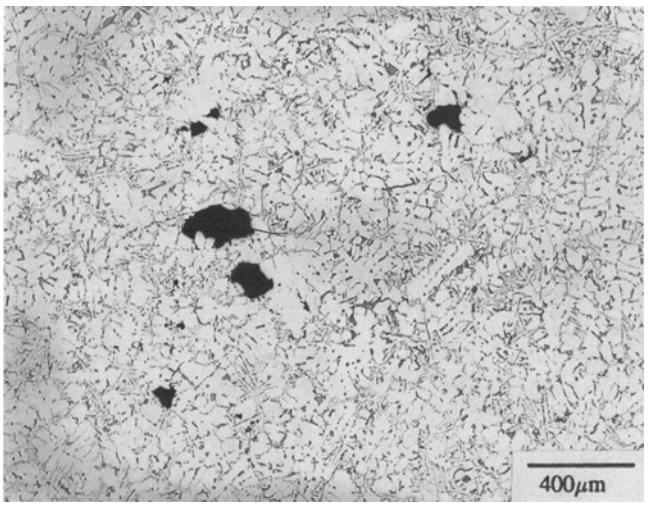

(*a*)

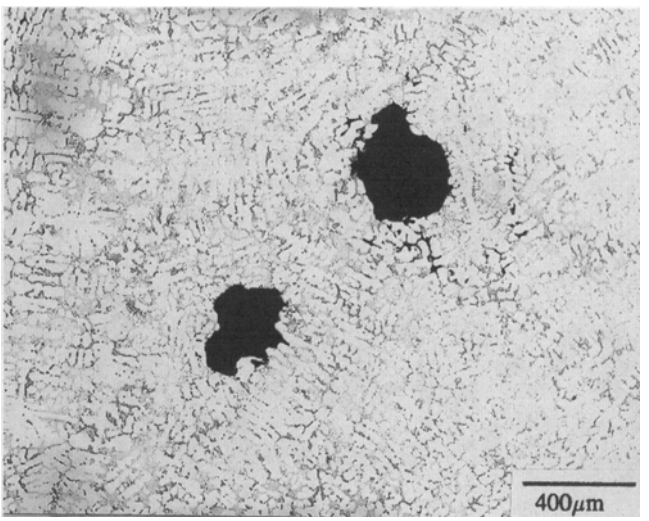

(*b*)

Fig. 17—Effect of Mg addition on pore size and density in (*a*) s7L alloy and (*b*) h5L alloy.

pared to h3 alloy (hydrogen level ~0.49 mL/100 g Al). It is interesting to note that the addition of strontium to Mg-containing alloy leads to a further decrease in percentage porosity. This is shown in Figure 18(a) obtained from s3 alloy ($t_s \sim 71$ seconds). The reason is not yet understood. The combined effect of Mg and the grain refining agent (TiB2) in minimizing percent porosity in high hydrogen-containing alloys is displayed in Figure 18(b), featuring porosity in h8 alloy solidified under the same conditions as those used to obtain the microstructure of h3L alloy shown in Figure 3(b).

2. *Zinc*

Zinc has a relatively high solubility in aluminum both at high and low temperatures. A zinc level of up to 3 wt pct has been reported to improve high-temperature properties and alloy machinability.

The role of zinc in porosity formation is not clear. It is believed that zinc may combine with phosphorus to form Zn_3P_2.[37] Figure 19 obtained from f5 alloy ($t_s \sim 71$ seconds) indicates that this combination enhances the pore size as

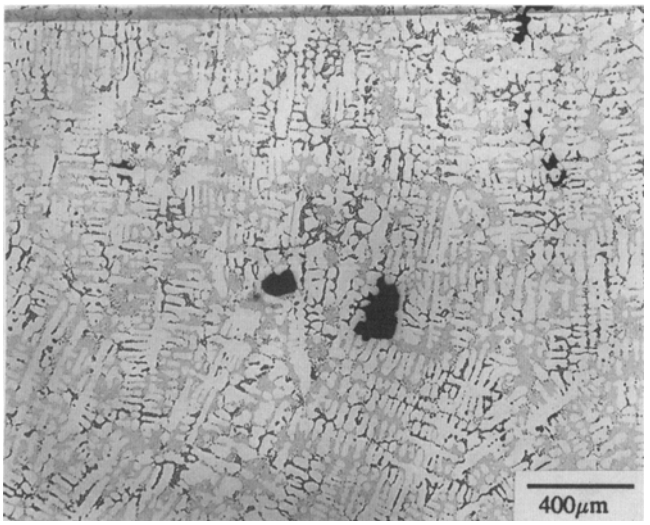

(*a*)

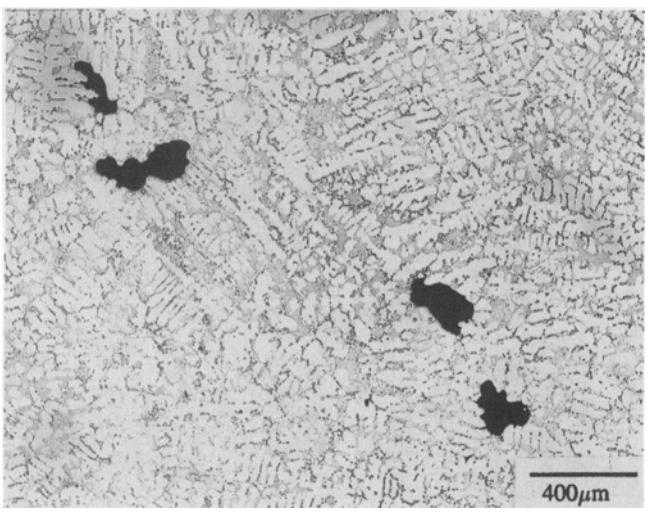

(*b*)

Fig. 18—Effect of (*a*) Mg + Sr (s3L alloy). (*b*) Mg + GR (h8L alloy) on pore size and distribution; GR = grain refiner.

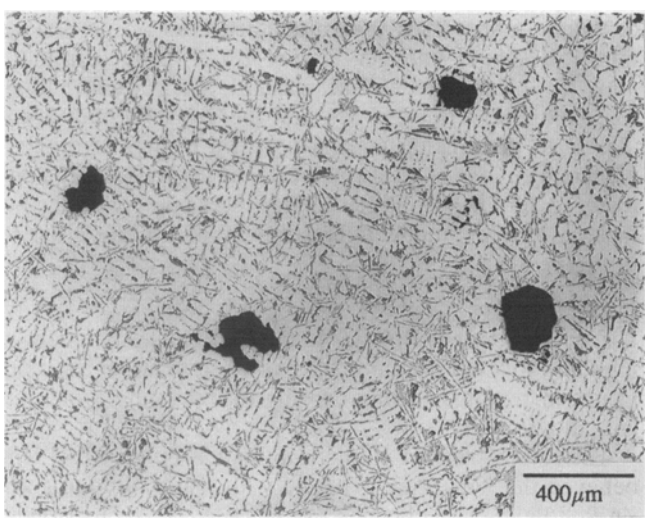

Fig. 19—Effect of a (Zn + P) combination on increasing the pore size in f5L alloy.

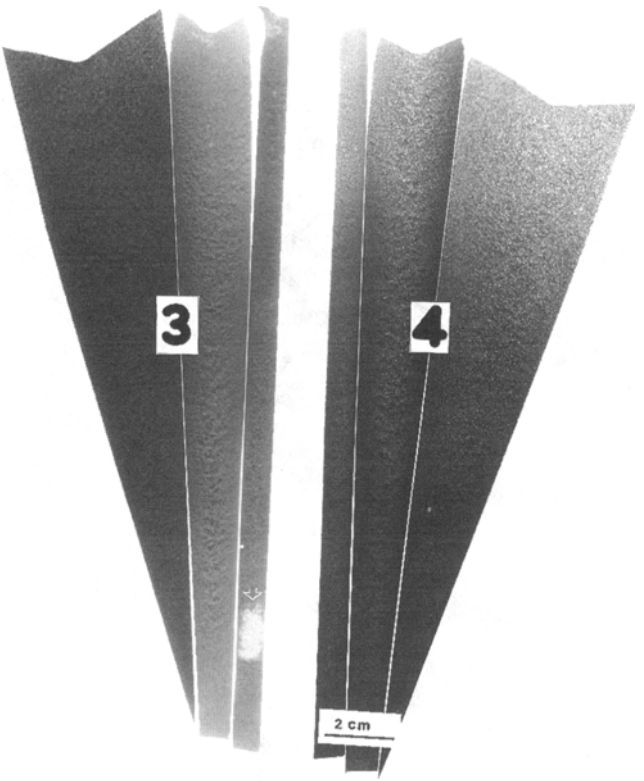

Fig. 20—X-ray radiographs obtained from h6 alloy: (*a*) series 3, corresponding to cold mold; and (*b*) series 4, corresponding to hot mold.

compared to f1 and f2 alloys containing 0 and 19 ppm phosphorus, respectively, and obtained under similar solidification conditions (Figures 6(b) and 10).

E. *Thermal Parameters*

1. *Solidification time (t_s)*

For a given hydrogen level, increasing the local solidification time is reported to increase percent porosity, pore length, and pore area.[38] This observation is consistent with the hypothesis that growth of microporosity is diffusion controlled, as demonstrated in Figures 3(a) and (b).

2. *Solidus velocity (V_s)*

The findings of Tynelius on A356 alloy[25] show that all porosity parameters increase with solidus velocity, when the eutectic grows with an equiaxed morphology, as opposed to planar front. This is explained as the effect of two nonexclusive phenomena, *viz.*, a reduced metal pressure when the permeability of the solid-liquid zone decreases and an expansion of pores in isolated liquid pockets during the volumetric contraction of the last liquid to solidify. The isolated liquid pockets may be described as microhot spots.

Two series of castings were prepared from the same melt (corresponding to h6 alloy, with a melt hydrogen level ~0.12 mL/100 g Al) and poured into the mold kept at three different wedge angles, *viz.*, 0, 5, and 15 deg, and maintained at mold temperatures of 25 °C and 300 °C, corresponding to series 3 and 4, respectively. Longitudinal slices (1-cm thick) were cut (passing through the mold centerline), polished, and examined by X-ray radiography. Figure 20 depicts radiographs that show the porosity distribution in the cold (series 3) and hot (series 4) molds. At the highest solidus velocity, porosity due to hot tearing is seen in

Table AI. Average and Maximum Pore Areas for Small (S) and Large (L) Samples

	Pore Density vs Pore Area Distribution Curve			
	Exponential Part		Irregular Part	
Alloy Sample	Average Value (μm^2)	Maximum Value (μm^2)	Average Value (μm^2)	Maximum Value (μm^2)
f1S	54.00	258.0	4,902.0	22,601.0
f1L	74.75	305.0	15,913.0	57,630.0
f2S	66.00	258.0	4,666.0	142,348.0
f2L	67.00	321.0	8,988.0	105,665.0
f3S	54.00	271.0	741.0	3,465.0
f3L	72.0	341.0	1,963.0	27,501.5
f4S	64.00	291.0	1,213.0	11,061.0
f4L	58.0	248.0	4,245.5	101,841.5
f5S	67.0	248.0	3,085.0	35,277.0
f5L	99.0	434.0	6,753.0	83,270.0
f6S	50.0	250.0	7,200.0	48,148.0
f6L	64.00	281.0	13,837.0	69,324.0
f7S	66.4	300.0	1,581.0	24,958.0
f7L	70.0	316.0	3,747.5	85,184.5
f8S	55.0	769.0	2,093.0	32,216.0
f8L	81.0	352.0	2,831.0	27,099.5
h1S	65.0	271.0	972.0	6,087
h1L	85.5	354.0	1,525.0	7,851.5
h2S	52.00	219.0	8,781.0	83,819.0
h2L	66.5	343.0	23,991.5	397,341.5
h3S	58.0	248.0	15,847.0	83,911.0
h3L	62.0	259.5	43,615.0	153,917.0
h4S	50.5	248.0	644.0	3,588.0
h4L	63.5	284.0	1,449.0	26,390.0
h5S	66.0	271.0	13,522.0	105,494.0
h5L	63.0	310.0	25,369.5	50,471.5
h6S	59.5	248.0	1,218.0	11,704.0
h6L	73.00	321.0	1,796.0	45,827.5
h7S	49.5	250.0	486.0	1,821.0
h7L	61.0	331.0	921.0	5,556.0
h8S	57.5	269.0	7,837.0	45,750.0
h8L	57.5	281.0	15,186.0	39,448.9
s1S	83.00	321.0	2,620.0	23,170.0
s1L	120.0	286.0	9,860.0	58,302.0
s2S	64.00	283.0	3,784.0	20,042.0
s2L	75.0	341.0	14,406.0	69,706.0
s3S	42.0	196.0	507.0	2,512.0
s3L	98.0	364.0	2,169.0	29,277.0
s4S	78.5	331.0	2,497.0	26,458.0
s4L	67.5	305.0	4,011.0	26,168.0
s5S	63.0	279.0	3,178.0	26,561.0
s5L	66.5	469.0	8,352.0	89,648.0
s6S	67.00	248.0	2,320.0	13,399.0
s6L	106.5	429.0	6,813.5	217,915.5
s7S	58.0	227.0	1,515.0	18,011.0
s7L	89.5	372.0	4,191.5	12,790.4
s8S	52.0	239.0	918.0	5,036.0
s8L	70.0	290.2	2,679.0	48,989.0

series 3 (for a zero deg opening angle). Reducing the solidus velocity through increasing the mold temperature, mold angle, or both resulted in eliminating this effect.

IV. CONCLUSIONS

1. In terms of its effect on porosity formation (as measured by the percentage porosity), a 0.1 mL/100 g Al level of hydrogen in the melt can be considered approximately equivalent to ~185 ppm Sr.
2. Grain refiner particles are appropriate sites for pore nucleation, resulting in fine and well-distributed pores. Reducing the grain size (or increasing the total grain boundary facet length) is another parameter to be considered in reducing pore size in grain-refined materials.
3. Phosphorus, as the primary silicon refiner agent, also reduces pore size, but to a lesser extent than the grain refiner. Its combination with zinc leads to an opposite behavior.
4. The β-Al_5FeSi needles are very active sites for pore

Table AII. Average and Maximum Pore Lengths for Small (S) and Large (L) Samples

Alloy Sample	Pore Density vs Pore Length Distribution Curve			
	Exponential Part		Irregular Part	
	Average Value (μm)	Maximum Value (μm)	Average Value (μm)	Maximum Value (μm)
f1S	16.7	73.9	122.0	209.0
f1L	22.07	98.3	185.5	376.5
f2S	18.8	86.8	150.0	598.0
f2L	18.62	104.5	198.5	619.0
f3S	15.2	103.0	135.0	135.0
f3L	17.75	116.0	181.0	278.0
f4S	18.70	106.0	137.0	203.0
f4L	18.8	115.0	213.0	657.5
f5S	21.6	90.0	143.0	286.0
f5L	24.75	129.0	175.5	522.6
f6S	16.8	83.9	154.0	323.0
f6L	18.5	103.0	215.5	437.0
f7S	20.4	100	157.0	296.0
f7L	18.76	113.0	195.0	627.0
f8S	15.6	103.0	158.0	367.0
f8L	21.7	119.0	169.0	283.0
h1S	19.2	123.0	173.0	184.0
h1L	18.1	110.0	188.0	248.0
h2S	21.6	90.3	175.0	458.0
h2L	19.85	98.3	216.0	371.0
h3S	21.1	93.3	229.0	431.0
h3L	16.95	107.7	321.0	675.0
h4S	14.4	103.0	—	—
h4L	17.0	109.5	183.0	424.0
h5S	18.6	106.0	224.0	468.0
h5L	17.75	119.0	357.0	691.0
h6S	17.9	113.0	147.0	199.0
h6L	18.85	120.5	219.0	527.0
h7S	12.9	87.1	—	—
h7L	16.75	98.3	129.0	213.0
h8S	19.9	93.3	175.0	386.0
h8L	18.05	105.0	247.0	703.0
s1S	27.3	113.0	179.0	235.0
s1L	29.2	146.5	245.0	338.0
s2S	21.5	88.5	127.0	192.0
s2L	21.3	119.0	217.0	408.0
s3S	12.9	90.0	—	—
s3L	26.7	171.0	198.5	373.0
s4S	19.7	116.0	215.0	215.0
s4L	19.0	99.8	159.0	399.0
s5S	22.5	103.0	158.0	273.0
s5L	24.5	103.0	185.0	454.5
s6S	24.5	113.0	141.0	141.0
s6L	26.35	169.0	290.0	344.0
s7S	19.0	100.0	173.0	350.0
s7L	21.8	154.0	217.0	514.0
s8S	15.7	90.3	144.0	200.0
s8L	20.8	123.0	182.0	395.0

nucleation. Also, they limit the growth of both gas and shrinkage pores. Addition of Mn neutralizes the formation of β needles and, hence, pore nucleation. The two Mn-containing compounds, *i.e.*, the α-Chinese script iron phase and sludge, limit pore growth/expansion.

5. The Al_2Cu phase particles may assist in pore formation in the absence of β-Al_5FeSi needles. However, they are not effective in the presence of β needles.
6. Magnesium reduces percent porosity; its effect is more pronounced in combination with strontium or TiB_2. The mechanism is not yet understood.
7. Increasing solidification time increases both pore length and pore area since pore growth is a diffusion-controlled process. Increasing the solidus velocity apparently leads to a similar observation, although the reason is different. In this case, it is due to the formation of microhot spots.

ACKNOWLEDGMENTS

Financial support received from the Natural Sciences and Engineering Research Council of Canada (NSERC) and the Centre Québécois de Recherche et de Développement de l'Aluminium (CQRDA) is gratefully acknowledged.

REFERENCES

1. Q.T. Fang and D.A. Granger: *Am. Foundrymen's Soc. Trans.*, 1989, vol. 97, pp. 989-1000.
2. W.R. Opie and N.J. Grant: *Trans. AIME*, 1950, vol. 188, pp. 1237-41.
3. A.M. Samuel and F.H. Samuel: *J. Mater. Sci.*, 1992, vol. 27, pp. 6533-63.
4. F.O. Traenkner: *Modern Casting*, 1982, Oct., pp. 36-37.
5. J.A. Eady and D.M. Smith: *Mater. Forum*, 1986, vol. 9, p. 217.
6. G. Drossel, R. Mai, and O. Liesenberg: *Giessereitechnik*, 1981, vol. 27, pp. 167-70.
7. D. Argo and J.E. Gruzleski: *Am. Foundrymen's Soc. Trans.*, 1988, vol. 96, pp. 65-74.
8. D. Apelian, G.K. Sigworth, and K.R. Whaler: *Am. Foundrymen's Soc. Trans.*, 1984, vol. 92, pp. 297-307.
9. R. DasGupta, C.G. Brown, and S. Marek: *Am. Foundrymen's Soc. Trans.*, 1988, vol. 96, pp. 297-310.
10. J.E. Gruzleski, P.M. Thomas, and R.A. Entwistle: *Br. Foundryman*, 1978, vol. 71, pp. 69-78.
11. H. Iwahori, K. Yonekura, Y. Yamamota, and M. Nakamura: *Am. Foundrymen's Soc. Trans.*, 1990, vol. 98, pp. 167-73.
12. H. Shahani: *Scand. J. Metall.*, 1985, vol. 14, pp. 306-17.
13. M. Drouzy, S. Jacob, and M. Richard: *Fonderie*, 1976, vol. 355, pp. 139-47.
14. B. Closset and J.E. Gruzleski: *Am. Foundrymen's Soc. Trans.*, 1982, vol. 90, pp. 453-64.
15. N. Roy, P.R. Louchez, and F.H. Samuel: *Metall Mater. Trans. A*, 1995, in press.
16. N. Roy, L. Zhang, P.R. Louchez, and F.H. Samuel: *J. Mater. Sci.*, 1995, in press.
17. C.E. Ransley and D.E.J. Talbot: *J. Inst. Met.*, 1955–56, vol. 84, p. 445.
18. A.M. Samuel and F.H. Samuel: *J. Mater. Sci.*, 1994, vol. 29, pp. 3591-3600.
19. D.E.J. Talbot: *Int. Metall. Rev.*, 1975, vol. 20, p. 166.
20. F.O. Traenkner: *Modern Casting*, 1981, p. 44.
21. F. Weinberg and D.A. Hirschfeld: *Metall. Sci.*, 1979, vol. 13, p. 335.
22. T.S. Piwonka and M.C. Flemings: *Trans. TMS-AIME*, 1966, vol. 236, p. 1157.
23. *Porosity in Aluminum Foundry Alloys—The Effect of Modification*, Proc. Int. Symp. on Production and Casting of Aluminum, Montreal, 1988, C. Bickert, ed., Pergamon Press, New York, NY, 1988, pp. 263-82.
24. J. Charbonnier, J.J. Perrier, and R. Portalier: *AFS Int. Cast. Met. J.*, 1978, vol. 3, p. 87.
25. K.E. Tynelius: Ph.D. Thesis, Drexel University, Philadelphia, PA, 1992.
26. M. Garat and R. Scalliet: *Am. Foundrymen's Soc. Trans.*, 1978, vol. 87, pp. 549-62.
27. S. Murali, K.S. Raman, and K.S.S. Murthy: *Mater. Characterization*, 1994, vol. 33, pp. 99-112.
28. L. Backerud, G. Chai, and J. Tamminen: *Solidification Characteristics of Aluminum Alloys*, vol. 2, *Foundry Alloys*, AFS/SKANALUMINIUM, Des Plaines, IL, 1990, pp. 151-55.
29. R.W. Bruner: *Metallurgy of Die Casting Alloys*, SDCE, Detroit, MI, 1976, p. 25.
30. L. Ananthanarayanan, F.H. Samuel, and J.E. Gruzleski: *Am. Foundrymen's Soc. Trans.*, 1992, vol. 100, pp. 383-91.
31. J. Gorbrecht: *Giesserei*, 1975, vol. 62, pp. 263-66.
32. A.M. Samuel and F.H. Samuel: *Metall. Mater. Trans. A*, 1995, vol. 26A, pp. 2359-2372.
33. J.E. Vorren, J.E. Evensen, and T.B. Pederson: *Am. Foundrymen's Soc. Trans.*, 1984, vol. 92, pp. 459-66.
34. J.L. Jorstad: *Soc. Auto. Eng. Inc.*, 1978, pp. 1-13.
35. R. DasGupta, C.C. Brown, and S. Marek: *Am. Foundrymen's Soc. Trans.*, 1989, vol. 97, pp. 245-54.
36. D.L. Pan, C.S. Lin, and C.R. Loper: *Am. Foundrymen's Soc. Trans.*, 1990, vol. 98, pp. 735-46.
37. L.F. Mondolfo: *Aluminium Alloys: Structure and Properties*, Butterworth and Co., London, 1976.
38. K.E. Tynelius, J.F. Major, and D. Apelian: *Am. Foundrymen's Soc. Trans.*, 1993, vol. 101, pp. 401-09.